Accepted Manuscript

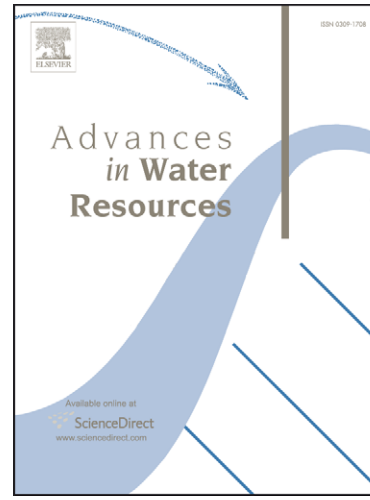

Computational issues and applications of line-elements to model subsurface flow governed by the modified Helmholtz equation

Mark Bakker, Kristopher L. Kuhlman

PII: S0309-1708(11)00034-0
DOI: 10.1016/j.advwatres.2011.02.008
Reference: ADWR 1667

To appear in: *Advances in Water Resources*

Received Date: 11 August 2010
Revised Date: 8 December 2010
Accepted Date: 10 February 2011

Please cite this article as: Bakker, M., Kuhlman, K.L., Computational issues and applications of line-elements to model subsurface flow governed by the modified Helmholtz equation, *Advances in Water Resources* (2011), doi: 10.1016/j.advwatres.2011.02.008

Computational issues and applications of line-elements to model subsurface flow governed by the modified Helmholtz equation

Mark Bakker

Water Resources Section, Faculty of Civil Engineering and Geosciences
Delft University of Technology, Delft, The Netherlands

Kristopher L. Kuhlman

Repository Performance Department
Sandia National Laboratories, Carlsbad, New Mexico, USA

Abstract

Two new approaches are presented for the accurate computation of the potential due to line elements that satisfy the modified Helmholtz equation with complex parameters. The first approach is based on fundamental solutions in elliptical coordinates and results in products of Mathieu functions. The second approach is based on the integration of modified Bessel functions. Both approaches allow evaluation of the potential at any distance from the element. The computational approaches are applied to model transient flow with the Laplace transform analytic element method. The Laplace domain solution is computed using a combination of point elements and the presented line elements. The time domain solution is obtained through a numerical inversion. Two applications are presented to transient flow fields, which could not be modeled with the Laplace transform analytic element method prior to this work. The first application concerns transient single-aquifer flow to wells near impermeable walls modeled with line-doublets. The second application concerns transient two-aquifer flow to a well near a stream modeled with line-sinks.

Key words: Analytic elements; Line elements; Transient flow; Laplace transform.

1 Introduction

Line elements are versatile building blocks for subsurface flow modeling using the analytic element method. They may be used to model many features, including stream segments, impermeable or leaky walls, and boundaries between zones with different aquifer properties. Historically, line elements have been used for the modeling of flow systems governed by Laplace's or Poisson's equation (e.g., [37]). More recently [8,4,26], line elements have been developed for flow systems governed by the modified Helmholtz equation. The general form of the modified Helmholtz equation is

$$\nabla^2\phi - \kappa^2\phi = 0 \tag{1}$$

Email addresses: mark.bakker@tudelft.nl (Mark Bakker), klkuhlm@sandia.gov (Kristopher L. Kuhlman).

where ϕ is a discharge potential, ∇^2 is the two-dimensional Laplacian operator, and κ is a parameter. For groundwater flow, the modified Helmholtz equation is often written as

$$\nabla^2\phi - \phi/\lambda^2 = 0 \tag{2}$$

where $\lambda = 1/\kappa$ is called the leakage factor. The simplest groundwater flow case governed by the modified Helmholtz equation is steady flow in a semi-confined aquifer, where λ may be computed from the aquifer and semi-confining layer properties (e.g., [37]). Transient flow in a single confined aquifer is governed by the diffusion equation, which may be transformed into the modified Helmholtz equation through a Fourier or Laplace transformation (e.g., [19,5,26]), in which case λ is generally complex. The system of differential equations governing steady flow in multi-aquifer systems may be separated into a set of independent modified Helmholtz equations using an eigenvalue analysis [23]. In the case of steady multi-aquifer flow there are as many λ values as there are aquitards. Transient multi-aquifer flow is a combination of the two former cases [24], where for the general case there are multiple complex λ values. Besides saturated flow, linearized steady unsaturated flow is also governed by the modified Helmholtz equation (e.g., [32], [7]).

The solution for a point sink (i.e., a well) or a dipole that satisfies the modified Helmholtz equation is well known and may be computed accurately for real and complex λ values at any distance from the well using Bessel function libraries. The solution for line elements is a different story, however. There are three approaches to derive equations for the potential of line elements. The first approach is based on the application of fundamental solutions in elliptic coordinates; these elements are referred to as elliptic line elements. The second approach requires integration of a point element along a line; these elements are referred to as integral line elements. The third approach is the relatively new generating analytic element approach [39] and is based on the repeated inversion of the Laplacian to obtain an infinite series of functions. In this paper, the first two approaches are applied. Both approaches may be applied to obtain the same type of boundary condition along a line element (e.g., specified normal gradient or jump in normal gradient), but the variation of the boundary condition along the element will be different. For example, the potential is continuous across a line-sink while the normal gradient is discontinuous. The variation of both the potential along the element and the jump in normal gradient across it differ between the two approaches. The two approaches are complementary. Depending on the problem at hand, it may be more advantageous to use one type of element over the other, as explained by [6].

Existing expressions for line elements that satisfy the modified Helmholtz equation cannot be computed accurately everywhere prior to this work (e.g., [8,6]). Evaluation of the potential for elliptic line elements is hampered by the ability to compute modified Mathieu functions with complex parameters at arbitrary distance from the element. Existing expressions for the potential for integral line elements cannot be evaluated at arbitrary distance from the element because either computation of the series suffers from round-off error or because adopted approximations are valid only within a region around the element. In addition, several existing expressions for integral line elements are valid only for real leakage factors. It is noted, however, that many of the existing expressions are perfectly suitable for simulation of, for example, steady flow in multi-aquifer systems, as this requires evaluation for real leakage factors up to a distance of 8λ only. For transient flow, the potential needs to be evaluated at much larger distances from the element, and preferably for complex λ.

The objective of this paper is two-fold. First, accurate approaches are presented for the evaluation of the potential function of elliptic and integral line elements, both with complex λ values, at any distance from the line element. Second, two new applications to transient flow are presented for these elements. The first concerns transient single-aquifer flow to a well near impermeable walls modeled with elliptic line-doublets. The second concerns transient two-aquifer flow to a well near head boundaries modeled with integral line-sinks. Both examples apply the Laplace-transform analytic element method [19,26], where analytic element solutions are obtained in the Laplace domain and the back transformation is computed numerically with the algorithm of de Hoog et al. [14].

2 Governing equations

Transient single-aquifer groundwater flow is governed by the diffusion equation (e.g., [37])

$$\nabla^2\phi = \frac{S}{kH}\frac{\partial\phi}{\partial t}, \tag{3}$$

where k is the hydraulic conductivity, H is the aquifer thickness (or the average saturated thickness for unconfined groundwater flow), S is the storage coefficient, also known as the storativity, t is time, and ϕ is the discharge potential

$$\phi = kHh \tag{4}$$

where h is the hydraulic head. Taking the Laplace transform of (3) gives

$$\nabla^2\Phi = \frac{pS}{kH}\Phi \tag{5}$$

where $\Phi = \mathcal{L}(\phi)$ and p is the Laplace transform parameter (generally complex); (5) is the same form as (2), when $\lambda = \sqrt{kH/(pS)}$. A solution for the potential in the physical time domain is obtained with the inverse Laplace transform, which may be expressed as the Bromwich contour integral

$$\phi = \mathcal{L}^{-1}\{\Phi\} = \frac{1}{2\pi i} \int_{\gamma - i\infty}^{\gamma + i\infty} \Phi e^{pt} \mathrm{d}p \tag{6}$$

A similar analysis may be carried out for transient flow in a multi-aquifer system. A detailed derivation for a system with an arbitrary number of aquifers is given in Hemker and Maas [24]. Here, discussion is limited to a two-aquifer system. Transient flow in a two-aquifer system is governed by

$$\nabla^2 \phi_1 = \frac{S_1}{T_1}\frac{\partial \phi_1}{\partial t} + \frac{\phi_1}{cT_1} - \frac{\phi_2}{cT_2} \tag{7}$$

$$\nabla^2 \phi_2 = \frac{S_2}{T_2}\frac{\partial \phi_2}{\partial t} - \frac{\phi_1}{cT_1} + \frac{\phi_2}{cT_2} \tag{8}$$

where T_n is the transmissivity of aquifer n. Storage in the separating layer is neglected here for brevity but may be included easily (see [24]). In Laplace space, the system of differential equations (7 and 8) may be written as a matrix differential equation

$$\nabla^2 \vec{\Phi} = \mathbf{A}\vec{\Phi} \tag{9}$$

where $\vec{\Phi}$ is a column vector with the Laplace-transformed potentials of aquifers 1 and 2 as its components, and

$$\mathbf{A} = \begin{pmatrix} 1/(cT_1) + pS_1/T_1 & -1/(cT_2) \\ -1/(cT_1) & 1/(cT_2) + pS_2/T_2 \end{pmatrix} \tag{10}$$

The eigenvalues of $\mathbf{A}$ are called w_1 and w_2 with corresponding eigenvectors $\vec{v}_1$ and $\vec{v}_2$. The general solution to the matrix differential equation (9) may now be written as

$$\vec{\Phi} = F_1\vec{v}_1 + F_2\vec{v}_2 \tag{11}$$

where the functions F_1 and F_2 satisfy the modified Helmholtz equations

$$\nabla^2 F_1 - w_1 F_1 = 0 \qquad \nabla^2 F_2 - w_2 F_2 = 0 \tag{12}$$

Comparison with (2) shows that $\lambda_1 = 1/\sqrt{w_1}$ and $\lambda_2 = 1/\sqrt{w_2}$, where both leakage factors are generally complex.

3 Laplace-transform analytic element method

There are several approaches to simulate transient flow with the analytic element method. Overviews for transient flow in single aquifers are given in [19,38,5,26]. A recent multi-aquifer transient analytic element approach using finite differences through time and distributed sources to represent the release from storage was presented by [18]. In this paper, solutions for transient groundwater flow are obtained with the Laplace-transform analytic element method [19,26].

The Laplace-transform analytic element method consists of three main steps. First, Laplace domain solutions are obtained through application of analytic elements that satisfy the modified Helmholtz equation (5 or 12). One solution is obtained for each value of the Laplace parameter p. Second, the analytic element solutions are evaluated to compute the transformed potential Φ at a point for multiple values of p. Third, the time-domain solution is found using the numerical inverse Laplace transform algorithm of de Hoog, et al., [14]. This method uses a doubly-accelerated Padé approximation to numerically integrate the Bromwich contour integral (6) that defines the inverse Laplace transform. Hence, it uses complex values of the Laplace parameter, p, and thus line elements need to be derived for complex λ values.

It is acknowledged that there are many algorithms for the numerical inversion of Laplace transforms (e.g., [13]). The Fourier-series based method of de Hoog, et al. [14], converges rapidly and works well with most general time behaviors, without ancillary parameters that need to be estimated (i.e., like the Weeks method [40]). The multiple values of p needed to estimate each $\phi(t)$ are not functionally related to t, allowing one set of $\Phi(p)$ values to be used to compute multiple $\phi(t)$ values, typically when t spans no more than a log-cycle. Alternative approaches, such as the Stehfest method [36], may require a unique set of $\Phi(p)$ for each t desired, which can be a significant penalty for situations where many nearby time values are needed, e.g., for particle tracking.

4 Elliptic line elements

The potential due to a line sink (continuous potential, discontinuous normal gradient) or line doublet (continuous normal gradient, discontinuous potential) may be developed in elliptical coordinates (Figure 1), using the special functions that arise from separation of variables (e.g., [29, p. 1407-1432]). A line segment of length L may be represented as an ellipse of zero radius (analogous to treating a point as a circle of zero radius). The solution for the potential is represented as an infinite sum of the product of similar-parity angular and radial Mathieu functions (i.e., no products of even and odd pairs). The coefficients for these elements are determined from boundary conditions, as is standard in the analytic element method (e.g., [38]). Coefficients can sometimes be computed analytically for simple boundary conditions and configurations (e.g., see unsaturated line source solution [27] and uniform strength line sink solution [26]).

The potential due to an elliptic line element is expanded in terms of elliptical eigenfunctions as

$$\Phi(\eta,\psi) = \sum_{n=0}^{\infty} \hat{a}_n \mathrm{Ke}_n(\eta;-q)\,\mathrm{ce}_n(\psi;-q) + \sum_{n=1}^{\infty} \hat{b}_n \mathrm{Ko}_n(\eta;-q)\,\mathrm{se}_n(\psi;-q) \tag{13}$$

where 'Ke' and 'Ko' are the even and odd second-kind modified radial Mathieu functions in terms of the Mathieu parameter $-q$, defined as

$$q = -\left(\frac{L}{4\lambda}\right)^2 = -\frac{1}{4\Lambda^2}. \tag{14}$$

where L is the length of the line-sink and $\Lambda = 2\lambda/L$. Furthermore, $\hat{a}_n$ and $\hat{b}_n$ are free coefficients to be determined, and 'ce' and 'se' are the even and odd first-kind modified angular Mathieu functions. The angular functions derive their names from "sine-elliptic" and "cosine-elliptic"; they are also referred to as Qe and Qo (e.g., [2]). The first summation represents an elliptic line-sink, while the second summation concerns an elliptic line-doublet (e.g., [6]). Other applications of Mathieu functions to model subsurface flow with analytic elements were presented by [7,4].

Operationally, the elliptic line elements are normalized by the value of the radial Mathieu functions at $\eta = 0$ to keep the Mathieu function products less than unity, resulting in

$$\Phi(\eta,\psi) = \sum_{n=0}^{\infty} a_n \frac{\mathrm{Ke}_n(\eta)}{\mathrm{Ke}_n(0)}\,\mathrm{ce}_n(\psi) + \sum_{n=1}^{\infty} b_n \frac{\mathrm{Ko}_n(\eta)}{\mathrm{Ko}_n(0)}\,\mathrm{se}_n(\psi) \tag{15}$$

where a_n and b_n are different free coefficients due to the normalization. The dependence of all the Mathieu functions in (15) on the same value of the Mathieu parameter, $-q$, is implicit. Expressions for the modified Mathieu functions used here are given in the Appendix.

5 Integral line elements

Equations for line-elements that fulfill the modified Helmholtz equation may alternatively be obtained through integration of point elements. The potential for a line-sink may be obtained through integration of a point sink along a line while the potential for a line-doublet may be obtained through integration of a doublet along a line (e.g., [37,6]). Equations for integral line elements are generally derived in a local X, Y coordinate system in which the line element lies along the X axis with its center at the origin and its end points at $X = -1$ and $X = +1$. The transformation from the x, y system to the X, Y system is carried out in complex form as

$$Z = X + iY = \frac{2z - (z_1 + z_2)}{z_2 - z_1}. \tag{16}$$

The potential for a line-sink with uniform inflow a may be written as (e.g., [8])

$$\Phi = -\frac{aL}{4\pi} \int_{-1}^{1} \mathrm{K}_0(r/\Lambda) d\Delta \tag{17}$$

where $r = \sqrt{(X - \Delta)^2 + Y^2}$, K_0 is the second-kind modified Bessel function of order zero, and as before $\Lambda = 2\lambda/L$ where L is the length of the line-sink. The potential for a line-doublet with uniform strength b may be written as [6]

$$\Phi = -\frac{bY}{2\pi\Lambda} \int_{-1}^{1} \frac{\mathrm{K}_1(r/\Lambda)}{r} d\Delta \tag{18}$$

where K_1 is the second-kind modified Bessel function of order one. The parameters a and b are free parameters that may be chosen to meet the desired boundary condition at a point along the line element. Strengths that vary as a polynomial along the line element may be derived as well (e.g., [6]), but are not used here. This paper discusses the computation of integral (17); the presented approach may be applied to integral (18) in a similar manner.

Integration of (17) is not possible in closed form. Several authors have integrated polynomial or series representations of K_0, for real Λ, of the form

$$\mathrm{K}_0(r/\Lambda) = \sum_{n=0}^{N} = [2a_n \ln(r/\Lambda) + b_n](r/\Lambda)^{2n} \tag{19}$$

Heitzman [22] analytically integrated a polynomial approximation of K_0 that is valid up to a distance of 2Λ ([1], Eq. 9.8.5). Bakker and Strack [8] integrated a polynomial approximation that is valid up to 8Λ [12]. Gusyev and Haitjema [20] integrated the infinite series representation given in ([1], Eq. 9.6.13). Although this results theoretically in an exact solution, it is well known that this series representation is difficult to compute for larger values of r using finite-precision arithmetic [30]. For example, a relative accuracy of 1×10^{-8} can only be achieved up to $r = 8\Lambda$ for real Λ using double precision arithmetic. The computational approach presented in this paper may be applied to compute the integral at any distance from the element and for complex leakage factors.

Integral line-sinks may be used to model transient flow in multi-aquifer systems [8]. For one value of the Laplace parameter p, the potential for a line-sink in a two-aquifer system consists of the summation of the potential for two line-sinks with different λ values (functions F_1 and F_2 in (11)) multiplied with the corresponding eigenvectors. As the inflow along both line-sinks is uniform, their strengths a_1 and a_2 may be chosen to match any division of inflow between the two aquifers (e.g., [8]). Alternatively, the strengths may be chosen such that, for example, the heads in the two aquifers are equal.

6 Computational issues of elliptic line elements

Since Mathieu functions are the natural basis functions for elliptical shapes, the only two significant sources of approximation in a numerical implementation of (15) are the numerical approximations involved in the computation of the Mathieu functions and the truncation of the infinite series at a finite number of terms (similar to traditional Fourier series).

Numerical computation of Mathieu functions, although straightforward, can be computationally costly and involves two main steps. The first step is the computation of the Mathieu coefficients (eigenvectors) and Mathieu characteristic numbers (eigenvalues), which depend on an infinite matrix containing the Mathieu parameter q (14), which is here complex. No published libraries were available for evaluation of modified Mathieu functions of complex q prior to this work. The second step, once the characteristic values are computed, is the evaluation of the Mathieu function values for specific η or ψ, by evaluating truncated infinite series of trigonometric or modified Bessel functions. Both computational steps are discussed below.

The calculation of Mathieu coefficients and characteristic numbers is either done through truncation of a related infinite continued fraction (e.g., [2,17]) or through the more direct eigenvalue problem for a truncated infinite banded matrix (e.g., [15,35,34]). The continued fraction approach is more specialized to a certain range of Mathieu parameters and orders of Mathieu functions and is potentially faster than the matrix approach. Alhargan's C++ library [2] uses a tuned version of the continued-fraction approach and is very accurate, but it only handles real $q \leq 4n$, where n is related to the Mathieu function order. Shirts [34] compared both the continued fraction and matrix approaches for real q and non-integer orders; he found the continued fraction method faster, but considered both accurate enough for calculation of Mathieu functions. The matrix approach is used here because it is more general, simpler to program, requires no initial guess, and utilizes the LAPACK library for eigenvalues and eigenvectors – specifically, routine ZGEEV [3].

Series representations are used to compute the Mathieu functions. Angular Mathieu functions are represented by infinite series of trigonometric functions. Radial Mathieu functions can be represented in terms of infinite series of hyperbolic trigonometric functions, Bessel functions, or products of Bessel functions (e.g., [28, Chap. 2,8,13]). Only the series of Bessel function products converge for all values of η, and they converge more rapidly with increasing η [9]. The series are given in Appendix A.

The computational accuracy of the elliptic line elements is related to the number of terms used in the truncated infinite series involved in the computation of each Mathieu function evaluation (i.e., the highest value of r used in (21)–(24)). The infinite matrices from which the eigenvalues (Mathieu characteristic numbers) and eigenvectors (Mathieu coefficients) are computed (25), include q in the off-diagonals and a function of n^2 on the diagonal (e.g., [15,35,34]). Appendix A contains an example matrix used as input to the LAPACK routine ZGEEV, which results in the $A^{(2n)}$ matrix needed for evaluation of the even orders of even Mathieu functions ((21) and (23)).

The boundary condition along elliptic line elements is met by computation of the free parameters a_n and b_n in (15), which means the boundary condition function is represented by a finite series of angular Mathieu functions. The convergence of trigonometric series used to expand potentials on the circumference of a circle is well known. Gibbs' phenomenon plagues the expansion of discontinuous functions, but otherwise the process is numerically well behaved. Similarly, Mathieu functions can expand arbitrary functions along the circumference of an ellipse; the convergence of generalized Fourier series are similar to the more common trigonometric Fourier series, converging and diverging for the same types of functions (e.g., [29, p. 745]). For smooth functions, the convergence of generalized Fourier series are fast. The smoother the function being expanded, the faster the convergence [10, §2.6], and the smaller the error committed in truncating the infinite series of basis functions.

Due to their popularity and wide use, there are numerous convergence acceleration techniques for smoothing Gibbs' phenomena encountered with trigonometric series [11, §2.1.4]. General analogous methods do not exist for truncated series of angular Mathieu functions, but [16] successfully accelerated the expansion of a cylindrical wave function with Mathieu functions using a Shanks transformation. Specialized applications can potentially benefit from these techniques.

Shirts [34, Eqs. 2.1 and 2.2] derived a rational approximation for the size of (25) required for an accuracy of 10^{-12}, given $|q|$ and the maximum required order of Mathieu function. These rational curves give the required matrix size as a function of q and order. Although they were derived for real q and general (non-integer) order, they show good agreement with the current implementation for complex q and integer order. The maximum practical $|q|$ is effectively 10^4 (i.e., elements of lengths up to $L = 2|\lambda|10^4$), which corresponds roughly to 100×100 matrices. Larger matrices slow down the entire LT-AEM computation significantly, and the modified Bessel function library cannot accurately compute Bessel functions of arbitrarily high order for all η.

7 Computational issues of integral line-sinks

The main computational issue of integral line-sinks is the evaluation of integral (17). A two-tiered approach is used to evaluate the integral accurately: near the element the integral is computed through analytic integration of a series representation, while farther from the element the integral is computed numerically using Gaussian Quadrature.

For evaluation purposes, the integral is divided into sections that are at most 3Λ long; if the line-sink is shorter than 3Λ no division is needed. Each section has its own local Z coordinate system. Within a circle of radius $|Z| < 3$, the integral is evaluated through analytic integration of the series representation K_0 presented in ([1], Eq. 9.6.13); formulas for the analytic integration are given in [8]. Along the circle $|Z| < 3$, the series representation of $\mathrm{K}_0(\sqrt{[(X-\Delta)^2 + Y^2]}/\Lambda)$ has a relative accuracy better than 10^{-10} using 18 terms in the series for a section of length 3Λ, and with less terms for shorter sections.

Outside the circle $|Z| = 3$, the integration is computed using Gaussian Quadrature. Along the circle $|Z| = 3$ a relative error less than 10^{-10} may be achieved using 7 Gauss-Quadrature points for a section of length 3Λ, and again with less terms for shorter sections. For the Gaussian Quadrature integration, the modified Bessel function K_0 is computed using the standard routine provided by the SciPy package for Python [33].

8 Performance of inverse Laplace transform algorithm

When working with a Laplace-transformed analytic element solution, the solution for a given value of t is computed from a set of solutions corresponding to a vector of values of p needed for the numerical inversion algorithm. For elliptic line elements, each value of p results in a different value of q, which requires calculation of the Mathieu characteristic numbers and Mathieu coefficients (i.e., eigenvalues and eigenvectors of (25)). When using the matrix approach to compute Mathieu characteristic numbers, this step is not easily parallelized or vectorized with the existing LAPACK library. For integral line elements used to model multi-aquifer flow, each value of p results in a different matrix $\mathbf{A}$ (Eq. 10), for which eigenvalues and eigenvectors need to be computed. For both sets of elements, a separate analytic element solution in Laplace space must be computed for each value of p to obtain values for the free parameters. Once the free parameters have been computed (one set for each value of p), computation of potentials and fluxes at various x, y, t locations are independent.

As mentioned, the numerical inverse Laplace transform algorithm by de Hoog, et al. [14] allows for inversion of several times within a single log-cycle of time, using a single vector of optimal p-values and $\Phi(p)$ as inputs. The expression used to pick a vector of p-values for a maximum value is

$$\mathbf{p} = \alpha - \frac{\ln(\epsilon)}{2T} + \frac{\pi j}{T} i \quad j = 0, 1, \ldots, N-1 \tag{20}$$

where α is the real portion of the greatest Laplace-domain singularity, ϵ is a desired tolerance, T is a scaling parameter (often chosen simply as $2t_{\max}$), N is the number of terms in the approximation, and i is the imaginary unit.

The fact that $\mathbf{p}$ is not directly a function of t allows the Laplace-space calculations for one t to be re-used at subsequent t within the same log-cycle. The calculation at individual x, y locations can either be parallelized across multiple processors, or the set of calculations can be vectorized on a single processor. Code vectorization involves significant re-writing of code (from an initial serial loop-based algorithm), while parallelizing a loop over locations can often be fairly simple. For example, the implementation of the Laplace transform AEM used here for elliptic elements is in Fortran95, allowing ready parallelization using OpenMP directives.

9 Examples of transient elliptical line-doublets

The following two examples illustrate the use of transient elliptical line-doublet elements and a specified zero normal flux boundary condition ($\partial\Phi/\partial\eta = 0$). Figure 2 shows a snapshot of heads and flow vectors in a transient system, where the effects of pumping have clearly developed around and between four impermeable barriers, represented with elliptical elements (heavy straight lines in the plots). This figure shows how the contours of head and flow vectors are modified by the presence of the line-doublets, compared to radially-symmetric flow to a pumping well in a homogeneous field. Head contours are perpendicular to barriers and vectors are parallel to them. The four openings between the barriers force the flow to constrict, increasing the flow velocity there. Stagnation points occur at the centers of the barriers; the low velocity zone around the stagnation points on the outsides of the barriers are clearly visible. In this case, the drawdown is propagating out towards large distances, as there is a net inflow into the model. In this example, 21 terms are used in the inverse Laplace transform algorithm, the infinite series of Mathieu functions (15) is truncated at 12 terms, and the matrix used for computing Mathieu functions (25) is truncated at 20 terms.

Figures 3 and 4 show an arrangement of impermeable barriers and an equal-strength pair of pumping and injection wells, with injection beginning first. The system is shown in an early transient state in Figure 3 with only the point source. The effects of the same line-doublets and point source, and an additional point sink are shown after pumping begins in Figure 4. Figure 5 is a plot of the time-evolution of head at two locations (stars in Figures 3 and 4). The time evolution plot consists of 200 time evaluations across 4 log-cycles of time; each log-cycle of time required 41 Laplace-space LT-AEM solutions (i.e., 164 solutions for a_n and b_n). Initially, the point source causes the head to rise at both locations. The additional drawdown due to the point sink is observed after $t = 0.75$. At the observation point closest to the point sink, the initial rise of the head quickly becomes a drawdown after the point sink starts (lower curve). For large time, the heads approach steady state, because extraction is balanced by injection.

Figures 3 and 4 show the case where four particles are released in the domain at the same time and tracked in the transient flowfield using an adaptive Runge-Kutta-Merson integration scheme with a specified error tolerance (e.g., see [31, §16.2]). Figure 3 shows the portions of the particle tracks up to the time associated with the contours. All three figures (3-5) illustrate the changing nature of drawdown and flow both around the impermeable obstacles (e.g., particles in late-time plot) and through time (comparison of early and late time contours and time-series head plot).

Many of the same features are visible in this example, compared to the symmetric example in Figure 2: the constriction between line-doublet elements increases flow, and stagnation points appear along the impermeable lines, changing their positions between the early and late plots.

In this example, the infinite generalized Fourier series is truncated at 12 terms, the Mathieu function matrix is truncated at 20, and 41 terms are used in the Fourier series inverse Laplace transform solution. More terms are used in the numerical inverse Laplace transform than in the previous example, to better represent the two separate step time behaviors (the point source at $t = 0$, the point sink at $t = 0.75$). Minor evidence of Gibbs' phenomenon due to the numerical Laplace transform inversion is visible immediately surrounding the yet-to-be-activated point sink in Figure 3, due to the dense grid of calculation points ($100{\times}100$, 16 times more points than the number of velocity vectors shown) and the small contour intervals used. As in any Fourier series representation of discontinuous processes (here a step in time), the Gibbs' phenomena can be isolated to an arbitrarily small region of time by increasing the number of terms in the Fourier series expansion, but they cannot be eliminated. For this case, superposition of two separate solutions, one for the point source and one for the point sink, would eliminate this behavior, but would be computationally twice as costly.

10 Examples of transient integral line-sinks in a two-aquifer system

Two examples are presented for transient flow to integral line-sinks in a two-aquifer system. The first example is for a situation with two aquifers with equal properties separated by a leaky layer. The top aquifer contains one line-sink that starts extracting water at time $t = 0$. At the same time, a line-source in the bottom aquifer starts to inject an equal amount of water. The line-source in the bottom aquifer is rotated 90° with respect to the line-sink in the top aquifer. Equipotentials in the top aquifer are shown at an early time ($t = 0.1$ d) and at a late time ($t = 10$ d) in Fig. (6); the same contour levels are used in both plots. The equipotential pattern is the same in the bottom aquifer but is rotated by 90°. Potentials as a function of time at two points in the top aquifer are shown in Fig. (7); potentials in the bottom aquifer have equal magnitude but opposite sign. Figure (6) shows that the tangent to the equipotentials in the top aquifer is discontinuous when crossing the line-sink in the top aquifer as the line-sink takes water from the top aquifer. The tangent is continuous, however, when crossing the location of the line-source in the bottom aquifer (the dashed line) as the dashed line-sink doesn't take water from the top aquifer. As explained in Section 7, near the line-sinks the integral (17) is evaluated differently than farther away. The transition occurs at different distances from the line-sink, depending on the values of t, and therefore λ, but is highly accurate and not visible in the equipotentials.

The second example of integral line-sinks demonstrates the ability to simulate the effect of pumping wells near rivers in a two-aquifer system. Consider a well that starts pumping near a meandering river in the top aquifer of a two-aquifer system. The effect of the well is modeled by simulating the deviation of the head from steady-state conditions (i.e., the opposite of the drawdown). As the head in the river is constant, the deviation is set equal to zero. The stream is simulated with 30 line-sinks. The top aquifer is modeled as unconfined with a phreatic storage coefficient that is 100 times as high as the storage coefficient of the bottom aquifer. The same constant transmissivity is used for both aquifers. A well starts pumping in the top aquifer at time $t = 0$ such that the drawdown at the well screen is constant and equal to unity for $t > 0$. A contour plot of the head in the top aquifer at an early and a late time is shown in Fig. 8; the contour interval is 0.02. The drawdown as a function of time is shown at three locations in Fig. 9 (Note the different vertical scales for the top and bottom aquifers). Points 1 and 2 are equal distance from the well, but the drawdown at point 2 is larger, as it is farther away from the river. The relative difference in drawdown between points 2 and 3 is much larger in the top aquifer than in the bottom aquifer, as there is a sharp cone of depression near the well in the top aquifer (where the well is screened) and not in the bottom aquifer.

11 Conclusions and Discussion

Two complimentary approaches were presented for the computation of the potential for line elements that fulfill the modified Helmholtz equation with complex leakage factors (see Eq. 2). Both approaches allow for the accurate computation of the potential at any distance from the element. The first approach is for elliptic line elements, which are combinations of Mathieu functions, while the second approach is for integral line elements, which are integrals of Bessel functions. Many groundwater flow fields are governed by the modified Helmholtz equation, or are governed by differential equations that may be transformed into the modified Helmholtz equation, including transient flow in single and multi-aquifer systems. The presented line elements were applied to obtain solutions for two transient flow systems that could not be modeled with the Laplace transform analytic element method previously: transient single aquifer flow with impermeable walls modeled with elliptic line-doublets, and transient two-aquifer flow with streams modeled with integral line-sinks.

As with other analytic element solutions, the tradeoff between accuracy and execution speed is relatively simple to adjust by increasing the number of terms used in expansions, increasing the number of terms retained in infinite series, or increasing the discretization of poly-lines. There is always a point of diminishing return, and the application will drive the required accuracy, and the time or locations where full accuracy may not be needed. For example, in the elliptical element formulation, increasing the number of terms in the generalized Fourier series expansion and Mathieu function matrix will increase spatial resolution. In the same implementation, the temporal resolution is controlled by the parameters in the inverse Laplace transform algorithm and will not necessarily be uniformly distributed in space; a single element may have more numerical error associated with the inverse Laplace transform than others, see Figure 3. The degree of accuracy at any location and time is a combination of all these effects. When a large number of spatial elements are included in a simulation, there may be locations where certain elements or groups of elements have negligible effect. A radius (or elliptical radius) may be determined, beyond which the element is skipped in the calculations.

There are a number of potential applications of the presented line elements, including application to multi-aquifer systems with an arbitrary number of aquifers and storage in the leaky layers (in essence extending the work for flow to wells in multi-aquifer systems of [24]), periodic flow in multi-aquifer systems (extending the work of [5]), and application to steady linearized unsaturated flow (extending the work of [7]). Extensions to the Laplace transform analytic element method that can be pursued include the modeling of well bore storage and skin effects to accommodate solving problems that arise in aquifer test analysis (commonly handled with radially symmetric analytic solutions) and the modeling of three-dimensional flow systems.

Acknowledgments

The authors thank James Craig and two anonymous reviewers for their comments which improved the quality of the final paper.

Development of the integral line-sinks was funded in part by Layne Hydro in Bloomington, IN. Integral line-sinks are implemented in the TTim code, which was developed at the Delft University of Technology for the US EPA Ecosystems Research division under contract QT-RT-10-000812 to SS Papadopulos in Bethesda, MD. The TTim code is available from code.google.com/p/ttim.

Sandia National Laboratories is a multi-program laboratory operated by Sandia Corporation, a wholly owned subsidiary of Lockheed Martin company, for the U.S. Department of Energy's National Nuclear Security Administration under contract DE-AC04-94AL85000.

References

[1] M. Abramowitz and I.A. Stegun. *Handbook of Mathematical Functions with Formulas, Graphs, and Mathematical Tables.* Dover, New York, 1964.

[2] F.A. Alhargan. Algorithms for the computation of all Mathieu functions of integer orders. *ACM Transactions on Mathematical Software*, 26(3):390–407, 2000.

[3] E. Anderson, Z. Bai, and C. Bischof. *LAPACK Users' guide*. Society for Industrial and Applied Mathematics, third edition, 1999.

[4] M. Bakker. Modeling groundwater flow to elliptical lakes and through multi-aquifer elliptical inhomogeneities. *Advances in Water Resources*, 27(5):497–506, 2004.

[5] M. Bakker. Transient analytic elements for periodic Dupuit-Forchheimer flow. *Advances in Water Resources*, 27(1):3–12, 2004.

[6] M. Bakker. Derivation and relative performance of strings of line elements for modeling (un)confined and semi-confined flow. *Advances in Water Resources*, 31(6):906–914, 2008.

[7] M. Bakker and J.L. Nieber. Two-dimensional steady unsaturated flow through embedded elliptical layers. *Water Resources Research*, 40(12):W12406, 2004.

[8] M. Bakker and O.D.L. Strack. Analytic elements for multiaquifer flow. *Journal of Hydrology*, 271(1–4):119–129, 2003.

[9] W.G. Bickley and N.W. McLachlan. Mathieu functions of integral order and their tabulation. *Mathematical Tables and Other Aids to Computation*, 2(13):1–11, 1946.

[10] J.P. Boyd. *Chebyshev and Fourier Spectral Methods*. Dover, second edition, 2001.

[11] C. Canuto, M.Y. Hussaini, A. Quarteroni, and T.A. Zang. *Spectral Methods in Fluid Dynamics*. Springer-Verlag, 1988.

[12] C.W. Clenshaw. *Mathematical Tables, Chebyshev series for mathematical functions, vol. 5. National Physical Laboratory*. Her Majesty's Stationary Office, London, 1962.

[13] A.M. Cohen. *Numerical Methods for Laplace Transform Inversion*. Springer, 2007.

[14] F.R. De Hoog, J.H. Knight, and A.N. Stokes. An improved method for numerical inversion of Laplace transforms. *SIAM Journal on Scientific and Statistical Computing*, 3(3):357–366, 1982.

[15] Delft Numerical Analysis Group. On the computation of Mathieu functions. *Journal of Engineering Mathematics*, 7(1):39–61, 1973.

[16] D. Erricolo. Acceleration of the convergence of series containing Mathieu functions using Shanks transformation. *IEEE Antennas and Wireless Propagation Letters*, 2:58–61, 2003.

[17] D. Erricolo. Algorithm 861: Fortran 90 subroutines for computing the expansion coefficients of Mathieu functions using Blanch's algorithm. *ACM Transactions on Mathematical Software*, 32(4):622–634, 2006.

[18] C.R. Fitts. Modeling aquifer systems with analytic elements and subdomains. *Water Resources Research*, 46(7):W07521, 2010.

[19] A. Furman and S.P. Neuman. Laplace-transform analytic element solution of transient flow in porous media. *Advances in Water Resources*, 26(12):1229–1237, 2003.

[20] M.A. Gusyev and H.M. Haitjema. An exact solution for a line-sink in the presence of leakage or transient flow. *Advances in Water Resources*, submitted 2010.

[21] J.C. Gutiérrez-Vega, R.M. Rodríguez-Dagnino, M.A. Meneses-Nava, and S. Chávez-Cerda. Mathieu functions, a visual approach. *American Journal of Physics*, 71(3):233–242, 2003.

[22] G. Heitzman. Analytical modeling of multi-layered groundwater flow. Master's thesis, University of Minnesota, 1977.

[23] C.J. Hemker. Steady groundwater flow in leaky multiple-aquifer systems. *Journal of Hydrology*, 72(3–4):355–374, 1984.

[24] C.J. Hemker and C. Maas. Unsteady flow to wells in layered and fissured aquifer systems. *Journal of Hydrology*, 90(3–4):231–249, 1987.

[25] C. Hunter and B. Guerrieri. Eigenvalues of Mathieu's equation and their branch points. *Studies in Applied Mathematics*, 64(2):113–141, 1981.

[26] K.L. Kuhlman and S.P. Neuman. Laplace-transform analytic-element method for transient porous-media flow. *Journal of Engineering Mathematics*, 64(2):113–130, 2009.

[27] K.L. Kuhlman and A.W. Warrick. Quasilinear infiltration from an elliptical cavity. *Advances in Water Resources*, 31(8):1057–1065, 2008.

[28] N.W. McLachlan. *Theory and Application of Mathieu functions*. Oxford, 1947.

[29] P.M. Morse and H. Feshbach. *Methods of Theoretical Physics*. McGraw-Hill, 1953.

[30] National Institute of Standards and Technology. Digital library of mathematical functions, May 2010. `http://dlmf.nist.gov/`.

[31] W.H. Press, S.A. Teukolsky, W.T. Vetterling, and B.P. Flannery. *Numerical recipes in FORTRAN; the art of scientific computing*. Cambridge University Press, 1993.

[32] A.J. Pullan. The quasilinear approximation for unsaturated porous media flow. *Water Resources Research*, 26(6):1219–1234, 1990.

[33] SciPy. Scientific tools for Python, July 2010. `http://scipy.org/`.

[34] R.B. Shirts. The computation of eigenvalues and solutions of Mathieu's differential equation for noninteger order. *ACM Transactions on Mathematical Software*, 19(3):377–390, 1993.

[35] J.J. Stamnes and B. Spjelkavik. New method for computing eigenfunctions (Mathieu functions) for scattering by elliptical cylinders. *Pure and Applied Optics: Journal of the European Optical Society Part A*, 4:251–262, 1995.

[36] H. Stehfest. Remark on algorithm 368: Numerical inversion of Laplace transforms. *Communications of the ACM*, 13(10):624, 1970.

[37] O.D.L. Strack. *Groundwater Mechanics.* Prentice Hall, 1989.

[38] O.D.L. Strack. Theory and applications of the analytic element method. *Reviews of Geophysics*, 41(2), 2003.

[39] O.D.L. Strack. The generating analytic element approach with application to the modified Helmholtz equation. *Journal of Engineering Mathematics*, 64(2):163–191, 2009.

[40] J.A.C. Weideman. Algorithms for parameter selection in the Weeks method for inverting the Laplace transform. *SIAM Journal of Statistical Computing*, 21(1):111–128, 1999.

Appendix A

The Mathieu functions used here are defined in terms of product series of Bessel functions. There are a large number of formulas, because there are even and odd functions, and even- and odd-order variants of each function. Further definitions and relations can be found in the Mathieu function literature [1,30,9]. The expressions for modified ($\Re(q) < 0$) Mathieu functions, when using the Morse normalization are (e.g., [29, p. 1409], [2])

$$\begin{aligned} \mathrm{ce}_{2n}(\psi) &= \sum_{r=0}^{\infty} A_{2r}^{(2n)} \cos\left[2r\left(\frac{\pi}{2}-\psi\right)\right] \\ \mathrm{ce}_{2n+1}(\psi) &= \sum_{r=0}^{\infty} B_{2r+1}^{(2n+1)} \sin\left[(2r+1)\left(\frac{\pi}{2}-\psi\right)\right] \end{aligned} \tag{21}$$

$$\begin{aligned} \mathrm{se}_{2n+1}(\psi) &= \sum_{r=0}^{\infty} A_{2r+1}^{(2n+1)} \cos\left[(2r+1)\left(\frac{\pi}{2}-\psi\right)\right] \\ \mathrm{se}_{2n+2}(\psi) &= \sum_{r=0}^{\infty} B_{2r+2}^{(2n+2)} \sin\left[(2r+2)\left(\frac{\pi}{2}-\psi\right)\right] \end{aligned} \tag{22}$$

$$\begin{aligned} \mathrm{Ke}_{2n}(\eta) &= \sum_{r=0}^{\infty} \frac{A_{2r}^{(2n)}}{A_0^{(2n)}} \mathrm{I}_r(\upsilon_1)\mathrm{K}_r(\upsilon_2) \\ \mathrm{Ke}_{2n+1}(\eta) &= \sum_{r=0}^{\infty} \frac{B_{2r+1}^{(2n+1)}}{B_1^{(2n+1)}} \left[\mathrm{I}_r(\upsilon_1)\mathrm{K}_{r+1}(\upsilon_2) - \mathrm{I}_{r+1}(\upsilon_1)\mathrm{K}_r(\upsilon_2)\right] \end{aligned} \tag{23}$$

$$\mathrm{Ko}_{2n+1}(\eta) = \sum_{r=0}^{\infty} \frac{A_{2r+1}^{(2n+1)}}{A_1^{(2n+1)}} \left[\mathrm{I}_r(v_1)\mathrm{K}_{r+1}(v_2) + \mathrm{I}_{r+1}(v_1)\mathrm{K}_r(v_2) \right] \tag{24}$$

$$\mathrm{Ko}_{2n+2}(\eta) = \sum_{r=0}^{\infty} \frac{B_{2r+2}^{(2n+2)}}{B_2^{(2n+2)}} \left[\mathrm{I}_r(v_1)\mathrm{K}_{r+2}(v_2) - \mathrm{I}_{r+2}(v_1)\mathrm{K}_r(v_2) \right]$$

where $v_1 = e^{-\eta}\sqrt{q}$, $v_2 = e^{\eta}\sqrt{q}$. The Morse normalization makes (23) and (24) simpler by enforcing $\mathrm{abs}(\mathrm{ce}_{2n}(0)) = 1$ on $A^{(2n)}$, $\mathrm{abs}(\mathrm{se}'_{2n+1}(0)) = 1$ on $A^{(2n+1)}$, $\mathrm{abs}(\mathrm{ce}_{2n+1}(0)) = 1$ on $B^{(2n+1)}$, and $\mathrm{abs}(\mathrm{ce}_{2n+2}(0)) = 1$ on $B^{(2n+2)}$. The columns of $A^{(2n)}$ are the eigenvectors of (25); there are similar matrices that result in the other A and B matrices [35].

$$\begin{bmatrix} 0 & q & 0 & 0 & 0 & \dots \\ 2q & 2^2 & q & 0 & 0 & \dots \\ 0 & q & 4^2 & q & 0 & \dots \\ 0 & 0 & q & (2n)^2 & q & \dots \\ \vdots & \vdots & \vdots & \vdots & \vdots & \ddots \end{bmatrix} \tag{25}$$

When $q = 0$, (25) is diagonal, and the eigenvalues are the square roots of the diagonal elements; $\mathrm{ce}_n(\psi)$ becomes $\cos(n\theta)$ and the line-element becomes a point. As q increases (e.g., as $t \to 0$, $|p| \to \infty$, or as L or KH/S increases), the matrix becomes less diagonally dominant, and the resulting Mathieu functions are less like sine/cosine functions (e.g., see Fig. 2 in [21]), requiring a larger matrix to approximate them and therefore more terms to approximate the Mathieu functions accurately. For both high orders and extremely large q, numerical cancellation will plague ZGEEV, regardless of matrix size (e.g., [34]). In the Mathieu function literature, it is recommended to use asymptotic expressions for the Mathieu characteristic numbers when q becomes very large, but their use for general q is complicated by the location of branch points and branch cuts in the complex q plane (e.g., [25]). The current implementation can accurately simulate a single line source with $q \leq 10^4$.

Figure captions

Figure 1. Elliptical coordinates; η is the radial coordinate, ψ is the azimuthal coordinate, a is the semi-major distance, and b is the semi-minor distance

Figure 2. Flow to a well with four impermeable barriers. Equally spaced contours of head at a snapshot in time (left), vectors indicating flow direction and magnitude – color fill proportional to $\log_{10}$ flow – at same time (right)

Figure 3. Early flow due to a point source. Equally spaced contours of head at $t = 0.7$ with early portions of four particle traces (left). At right, vectors indicating flow direction and magnitude at same time (color fill proportional to $\log_{10}$ flow); stars indicate locations of time series plots in Fig. 5

Figure 4. Flow between equal-strength opposite-sign point sink and source. Equally spaced contours of head at $t = 0.775$ with four particle traces (left). At right, vectors indicating flow direction and magnitude at same time (color fill proportional to $\log_{10}$ flow)

Figure 5. Time series of modeled head through time at two (x,y) locations: lower curve (closer to pumping well) at $(0.0,-0.1)$ and upper curve (closer to injection well) at $(-0.2,0.1)$. Injection began at $t = 0$, pumping began at $t = 0.75$.

Figure 6. One line-sink in top aquifer (solid black line) and one line-source in bottom aquifer (dashed black line). Equipotentials in top aquifer at $t = 0.1$ d (left) and $t = 10$ d (right). Same contour levels are shown in both plots.

Figure 7. Drawdown at two locations for case of Fig. (6).

Figure 8. Head contours in the top aquifer for a well located near a meandering river. Contours are shown at an early time (left) and a late time (right). Head at the well is -1, and contour interval is 0.02.

Figure 9. Drawdown at three locations in top aquifer (left) and bottom aquifer (right). Vertical scales differ between two graphs. Locations are shown in Fig. (8)

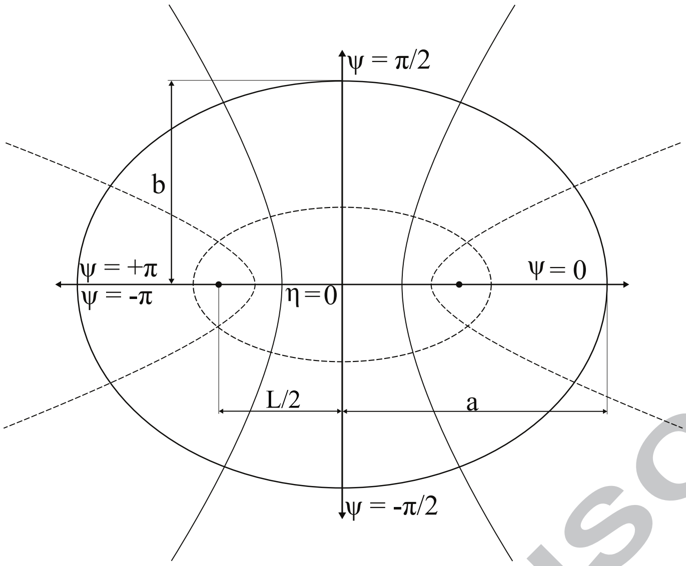

Fig. 1. Elliptical coordinates; η is the radial coordinate, ψ is the azimuthal coordinate, a is the semi-major distance, and b is the semi-minor distance

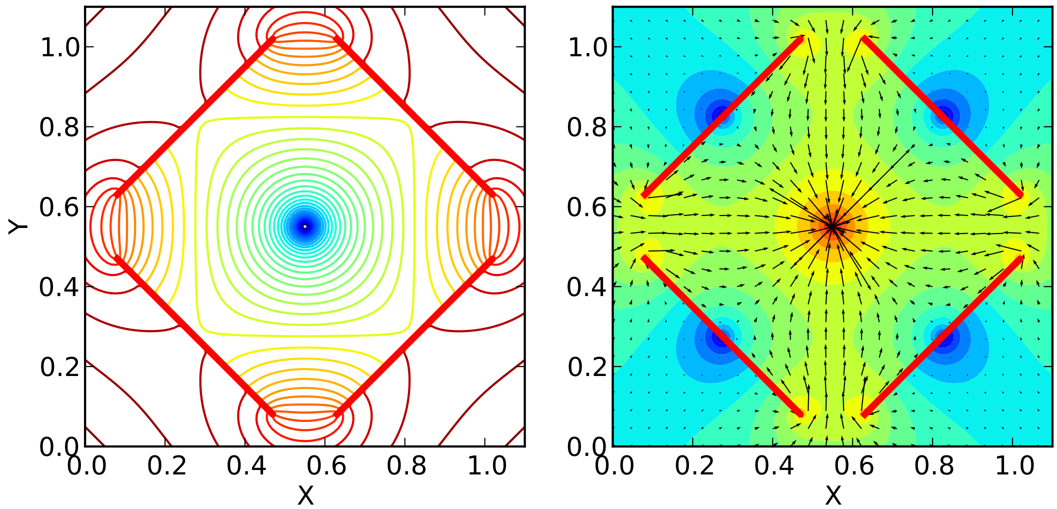

Fig. 2. Flow to a well with four impermeable barriers. Equally spaced contours of head at a snapshot in time (left), vectors indicating flow direction and magnitude – color fill proportional to $\log_{10}$ flow – at same time (right)

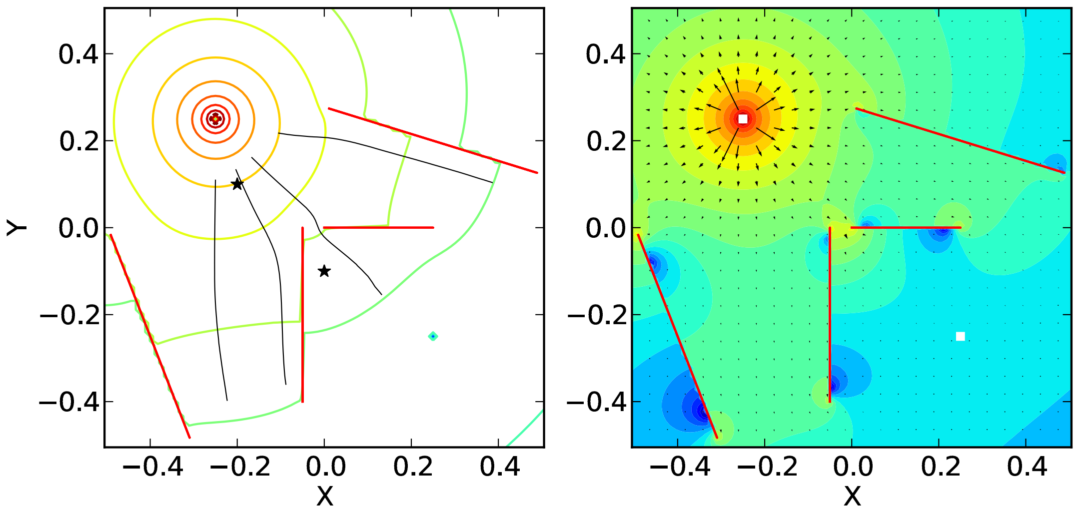

Fig. 3. Early flow due to a point source. Equally spaced contours of head at $t = 0.7$ with early portions of four particle traces (left). At right, vectors indicating flow direction and magnitude at same time (color fill proportional to $\log_{10}$ flow); stars indicate locations of time series plots in Fig. 5

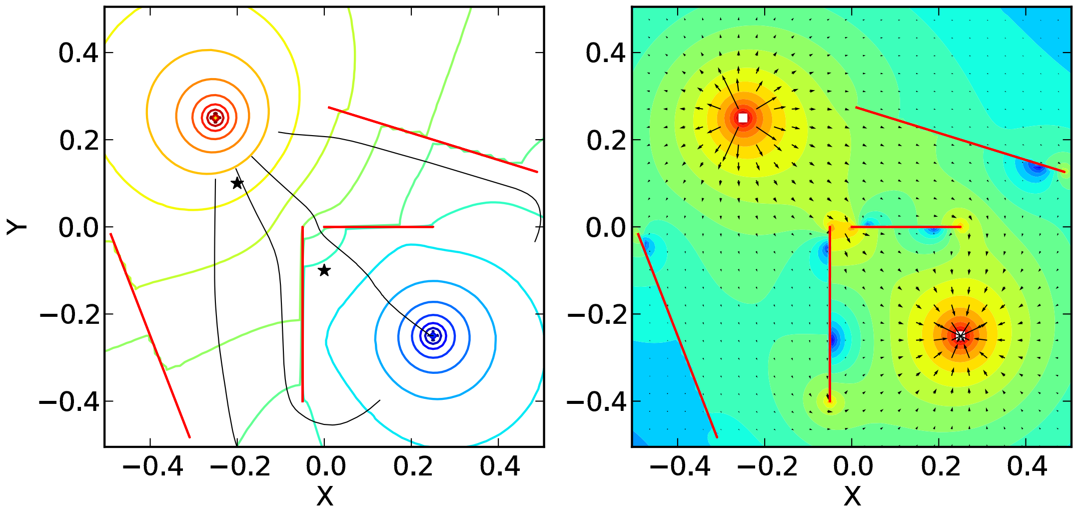

Fig. 4. Flow between equal-strength opposite-sign point sink and source. Equally spaced contours of head at $t = 0.775$ with four particle traces (left). At right, vectors indicating flow direction and magnitude at same time (color fill proportional to $\log_{10}$ flow)

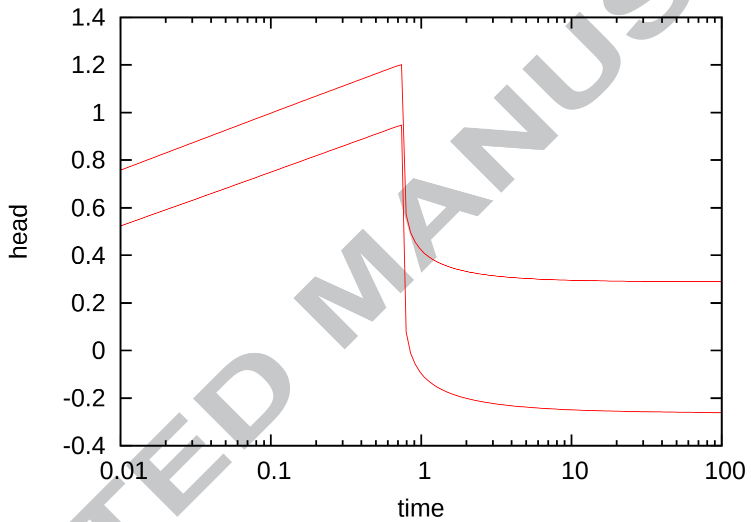

Fig. 5. Time series of modeled head through time at two (x,y) locations: lower curve (closer to pumping well) at $(0.0,-0.1)$ and upper curve (closer to injection well) at $(-0.2,0.1)$. Injection began at $t = 0$, pumping began at $t = 0.75$.

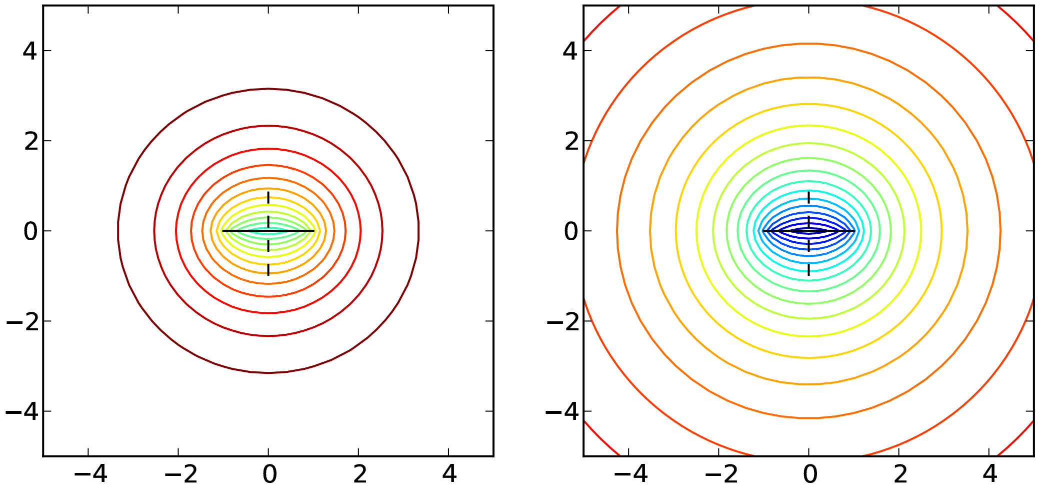

Fig. 6. One line-sink in top aquifer (solid black line) and one line-source in bottom aquifer (dashed black line). Equipotentials in top aquifer at $t = 0.1$ d (left) and $t = 10$ d (right). Same contour levels are shown in both plots.

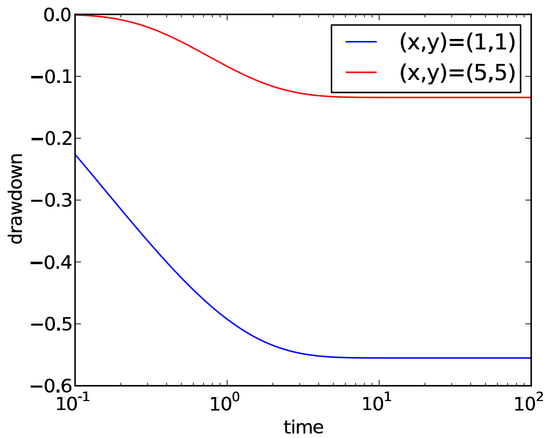

Fig. 7. Drawdown at two locations for case of Fig. (6).

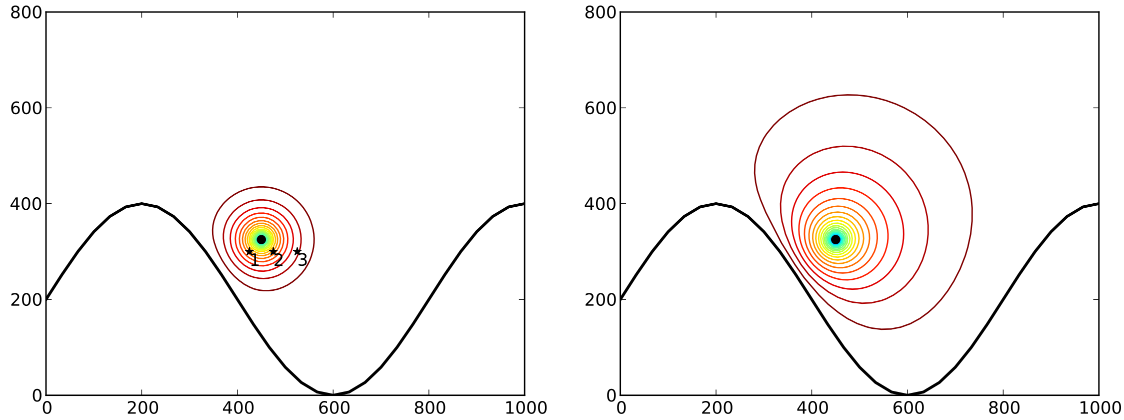

Fig. 8. Head contours in the top aquifer for a well located near a meandering river. Contours are shown at an early time (left) and a late time (right). Head at the well is -1, and contour interval is 0.02.

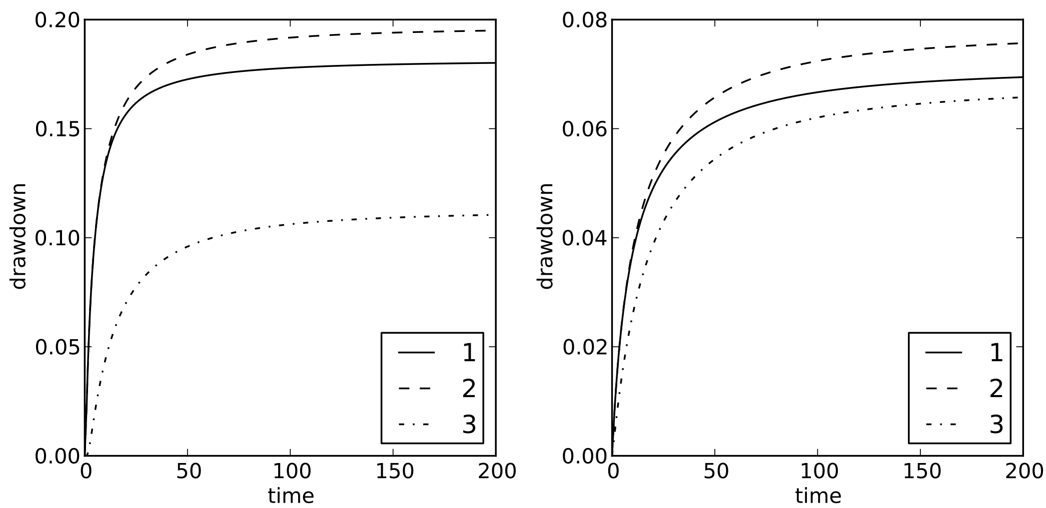

Fig. 9. Drawdown at three locations in top aquifer (left) and bottom aquifer (right). Vertical scales differ between two graphs. Locations are shown in Fig. (8)